Pergamon

Int. J. Heat Mass Transfer. Vol. 40, No. 10, pp. 2327–2339, 1997

0017–9310/97 $17.00+0.00

PII: S0017–9310(96)00298–0

An analytical model for near-saturated pool boiling critical heat flux on vertical surfaces

ISSAM MUDAWAR, ALICIA H. HOWARD and CHRISTOPHER O. GERSEY

Boiling and Two-phase Flow Laboratory, School of Mechanical Engineering, Purdue University, West Lafayette, IN 47907, U.S.A.

(*Received* 2 *July* 1996 *and in final form* 16 *August* 1996)

Abstract—Photographic studies of vertical pool boiling for near-saturated conditions were conducted in order to determine the critical heat flux (CHF) trigger mechanism. The studies revealed that, for heat fluxes near CHF, vertical pool boiling exhibits vapor behavior similar to that observed in flow boiling. At fluxes slightly below CHF, the Kelvin–Helmholtz instability creates a wavy layer at the liquid–vapor interface. The heater surface is wetted, and thus cooled, only by the wave troughs, referred to as wetting fronts, which repeatedly sweep across the surface. Prior to CHF, the curvature of the wetting front creates a pressure force which tends to preserve interfacial contact with the wall. Critical heat flux occurs when the pressure force due to interfacial curvature is overcome by the momentum of vapor at the site of the first wetting front, causing the interface to lift away from the wall. Once the first wetting front lifts off from the surface, the remaining wetting fronts separate from the surface in succession. It is shown that the interfacial lift-off criterion facilitates accurate theoretical modeling of CHF in vertical pool boiling, and produces an equation which is identical in form, but not mechanism, to traditional horizontal CHF models.

1. INTRODUCTION

Predicting CHF has been the focus of a considerable body of research spanning over four decades. Kutateladze [1] first addressed the problem by using dimensional analysis to prove saturated pool boiling CHF can be correlated in the form:

$$\frac{q_m}{\rho_g h_{fg}\left[\dfrac{\sigma(\rho_f-\rho_g)g_e}{\rho_g^2}\right]^{1/4}} = K \qquad (1)$$

where K is a constant and is hereafter referred to as the dimensionless critical heat flux. Based on a curve fit of data, Kutateladze recommended a value of K equal to 0.16 for pool boiling from a large horizontal flat plate. Since Kutateladze determined equation (1) from dimensional analysis alone, it is presumable that most theoretical CHF models for saturated pool boiling will produce equations similar in form to equation (1), regardless of the proposed CHF trigger mechanism.

Influenced by Kutateladze's work [1], Zuber *et al.* [2] utilized well-established hydrodynamic instability theory to determine the limits on liquid access to the wall and thus derived the above equation for pool boiling on an infinite horizontal surface, where K was found to equal $\pi/24$ or 0.131. The well known pool boiling CHF model of Zuber *et al.* has maintained its popularity because of its theoretical appeal. However, many attempts have been made to alter this model in order to account for effects the original model did not address, such as finite heater size, heater geometry, and surface orientation. The latter of these effects, particularly the case of a vertical surface, is the focus of the present study.

As a key element of the model, Zuber *et al.* [2] included the Taylor instability criterion, in addition to the Helmholtz instability criterion. Since the Taylor instability includes the gravitational force per unit mass normal to the heater surface, g_e should be replaced with g_n to account for orientation effects, where $g_n = g_e \cos\theta$. The effects of orientation on both the theoretical Zuber *et al.* model and on actual dimensionless CHF data are compared in Fig. 1. The orientation angle, θ, is measured from the horizontal position. The data presented in Fig. 1 were obtained during the current investigation, and the test facility and test procedure are described later in this paper. For a vertical surface, the gravitational force normal to the surface is zero, so the theoretical model by Zuber *et al.* predicts zero CHF. Conversely, experimental evidence proves CHF for this orientation and for all orientations between horizontal and vertical are only slightly smaller than CHF for a horizontal surface. Clearly, the Zuber *et al.* model does not accurately describe the data for a vertical surface. It is the key objective of the present study to develop a new model for pool boiling CHF on a vertical surface.

Table 1 summarizes the results of near-saturated vertical pool boiling studies identified for the present work. Experiments run with circular heaters were

NOMENCLATURE

b	wetting front span (length)
c	wave speed
c_p	specific heat at constant pressure
c_i	imaginary component of wave speed
c_r	real component of wave speed
f_g	wall friction factor
f_i	interfacial friction factor
g_e	Earth's gravity
g_n	component of gravitational force per unit mass normal to liquid–vapor interface
h_{fg}	latent heat of vaporization
H	mean layer thickness
k	wave number, $2\pi/\lambda$
k_c	critical wave number, $2\pi/\lambda_c$
K	dimensionless CHF defined in equation (1)
L	heater length
L'	dimensionless characteristic heater length defined in equation (23)
n	number of wetting fronts
P	pressure
$\overline{P_f - P_g}$	mean interfacial pressure difference in wetting front
q_l	localized heat flux in the wetting front
q_m	critical heat flux (CHF)
$q_{m,z}$	critical heat flux (CHF) predicted from the model by Zuber *et al.* [2]
$q_{m,0°}$	critical heat flux (CHF) for the horizontal upward-facing orientation
q_s	local heat flux
Re	Reynolds number
t	time
th	heater thickness
T	temperature
ΔT_{sub}	liquid subcooling
$\bar{u}$	mean velocity
w	heater width
z	spatial coordinate in the stream-wise direction
z^*	distance from leading edge of heater to center of first wetting front, $z^* = \lambda_c$.

Greek symbols

δ	mean vapor layer thickness
η	interfacial displacement
η_0	amplitude of interfacial displacement
λ	wavelength of interfacial perturbation
λ_c	critical wavelength corresponding to onset of instability
μ	viscosity
ρ	density
ρ''	modified density, $\rho'' = \rho\coth(kH)$
θ	orientation angle measured from the horizontal position
σ	surface tension
τ	wetting period
τ_g	wall shear stress
τ_i	interfacial shear stress.

Subscripts

f	saturated liquid
g	saturated vapor
m	mean
sub	subcooling.

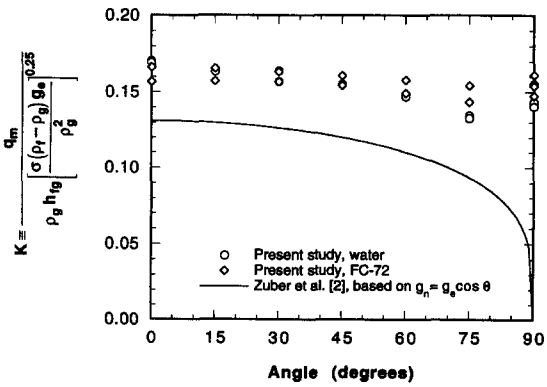

Fig. 1. Comparison of the model by Zuber *et al.* [2] with dimensionless pool boiling CHF data for different orientations.

omitted because the lack of a heater bottom edge introduces three dimensional effects which, even though usually considered small, are beyond the scope of this paper. Additionally, transient studies were omitted since they often produce reduced CHF values [3]. For completeness, the table also includes an empirical correlation by Lienhard and Dhir [4] for vertically oriented ribbon heaters insulated on one side.

Although fairly reliable empirical CHF correlations exist in the literature for a variety of heater sizes, shapes, and orientations, in recent years many researchers have refocused their efforts on determining the key physical mechanisms responsible for initiating CHF in pursuit of a universal CHF model. At high heat flux conditions leading to CHF, vertical pool boiling experiments exhibit vapor behavior that resembles flow boiling more than horizontal pool boiling. With regard to flow boiling, five main types of models have been proposed which encompass virtually all of the CHF research. These are *boundary layer separation* [10–12], *mechanical energy criterion* [13, 14], *bubble crowding* [15–17], *sublayer dryout* [18–

Table 1. Summary of previous literature on vertical pool boiling CHF

Reference	Fluid	$w \times L(\times th)$ [mm]	K†	Correlation	Comments
Lienhard and Dhir [4]	Methanol	Nichrome ribbons $101.6 \times 2.5(\times 0.2)$	0.156–0.170	$\frac{q_m}{q_{m,z}} = \frac{1.4}{(L')^{0.25}}$ for $L' < 6$‡	Small vertically oriented ribbons insulated on back side.
	Acetone	$101.6 \times 4.8(\times 0.2)$	0.135–0.140		Correlation based on eight data points. $q_{m,z}$ is the CHF value predicted from the model by Zuber *et al.* [2] based on g_e.
	Water (at high g-forces)	Nichrome ribbons 101.6×1.0 to $4.8(\times 0.2)$	0.118	$\frac{q_m}{q_{m,z}} = 0.90$ for $L' \geqslant 6$‡	Large vertically oriented ribbons insulated on back side. Correlation based on 24 high gravity data points obtained by Adams [5]. $q_{m,z}$ is the CHF value predicted from the model by Zuber *et al.* [2] based on g_e.
Vishnev *et al.* [6]	Liquid helium	Stainless steel $96 \times 10.4(\times 0.063)$	0.080–0.093	$\frac{q_m}{q_{m,0^\circ}} = \frac{(190-\theta)^{0.5}}{190^{0.5}}$	$q_{m,0^\circ}$ is the CHF value for the heater oriented in the horizontal upward-facing position ($\theta = 0^\circ$). $\theta = 90^\circ$ for a vertical surface.
Monde *et al.* [7]	Water	Copper heaters 10×20, 35 and 50	0.132–0.148		Effects of channel depth were investigated and a correlation was developed. The correlation converges to $K = 0.16$ for very large channel depths. Data indicated in this table are for 'infinite' channel depths only.
	Ethanol		0.135–0.155		
Beduz *et al.* [8]	Liquid nitrogen	Copper and aluminum heaters $50 \times 50(\times 6)$	0.117–0.214		Surface finishes of heaters were mirror polished, grooved and rolled, and plasma sprayed.
Chui *et al.* [9]	Liquid nitrogen	Copper heater $21.6 \times 17.4(\times 2.5)$	0.118		Heater surface roughness was 0.15 μm.

†$K = \dfrac{q_m}{\rho_g h_{fg}\left[\dfrac{\sigma(\rho_f - \rho_g)g_e}{\rho_g^2}\right]^{0.25}}$.

‡$L' = L\left[\dfrac{(\rho_f - \rho_g)g_e}{\sigma}\right]^{0.5}$.

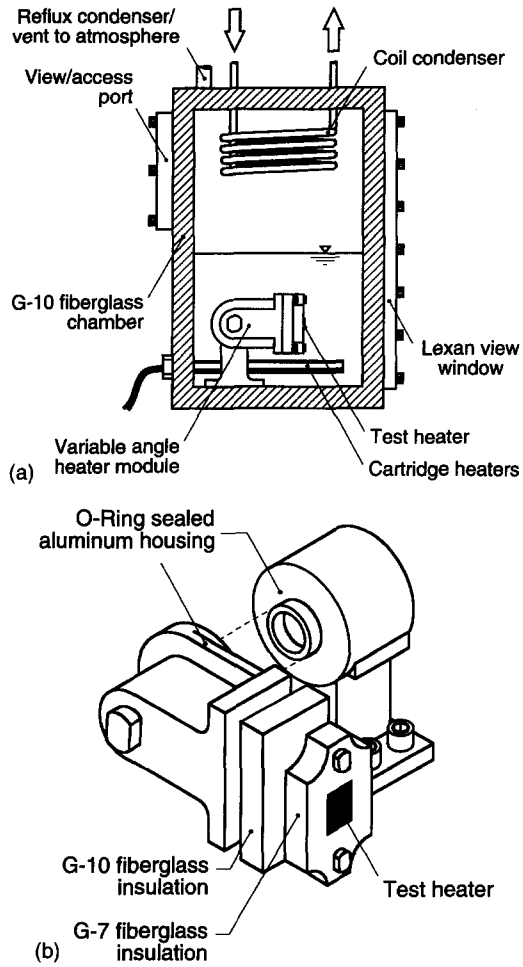

Fig. 2. (a) Pool boiling test facility and (b) angular rotation platform.

20], and *interfacial lift-off* [21–24]. The latter is the model discussed in the present paper.

Using an apparatus which lends itself to a high resolution photographic study of interfacial features, the present study will first show that the trigger mechanism for CHF from a vertical surface in near-saturated pool boiling is interfacial lift-off. This study will then treat pool boiling on a vertical surface as a limiting condition of flow boiling corresponding to zero liquid velocity, resulting in a simplified expression for vertical pool boiling CHF.

2. EXPERIMENTAL INVESTIGATION

2.1. *Pool boiling test facility and CHF orientation study*

Figure 2(a) shows a schematic of the pool boiling test chamber which was constructed of G-10 fiberglass plastic and fitted on the front and back with Lexan windows. The chamber was equipped with two condensers and three cartridge heaters. The condenser coil inside the chamber effectively recovered almost all of the vaporized liquid, and an external reflux condenser connected to the chamber's vent acted as a final barrier to any escaping vapor during both deaeration and testing. The cartridge heaters allowed the fluid to be dearated prior to testing and also maintained the bulk liquid at near-saturated conditions. To prevent the boiling on the cartridge heaters from influencing CHF on the primary test heater, the cartridge heaters were placed at the back of the test chamber and isolated from the test heater by a baffle plate (not shown).

For the orientation study, distilled water and FC-72, a 3M dielectric fluid, were tested at atmospheric pressure. The heater utilized to test FC-72 consisted of a 12.7×12.7 mm^2 copper block which was heated by a thick-film electrical resistor silver soldered to its back. A similar configuration was used for pool boiling of water but with a heater measuring 12.0 mm in width and 62.0 mm in length. Current and voltage transducers measured the heat flux and thermocouples placed just beneath the heater surface were utilized to infer the surface temperature of the heaters from a one-dimensional heat conduction model. Since the heaters were imbedded in insulative G-7 fiberglass plastic, heat losses through the heaters' sides and backs were found to be negligible. Each heater was mounted on an angular rotation platform shown in Fig. 2(b) to facilitate testing at different surface orientations. Further details of the pool boiling test facility can be found in ref. [25].

2.2. *Vertical pool boiling flow visualization facility*

The photographic portion of this investigation was conducted with FC-72 at 1 atm. Figure 3(a) shows a schematic of the heater module utilized during the flow visualization study. The heater module contained three 10-mm wide heaters with lengths of 10, 30 and 110 mm, and was used previously in near-saturated flow boiling CHF tests performed by Gersey and Mudawar [23]. As shown in Fig. 3(a), two transparent Lexan walls approximately 20 mm in height were added to the heater module to create a 10 mm wide gap directly above the heaters. This eliminated any side effects from liquid gaining access to the heater surface in the transverse direction. The module was oriented vertically inside a 150 mm $\times$ 250 mm rectangular pool boiling test facility similar in construction to the one shown in Fig. 2(a). Complete visual access to the heater surfaces was possible through the Lexan enclosure as well as the Lexan side walls on the heater module. Still pictures of the near-wall interfacial features were made with a 35-mm Nikon camera with a 200 mm lens and assorted attachments.

The 30 mm heater is shown in Fig. 3(b). The 10 and 110 mm heaters were similar in construction. The heaters were powered by thick-film resistors [Fig. 3(c)] that were silver soldered to the underside of the respective copper slabs: one resistor on the 10 mm heater, two on the 30 mm heater, and six on the 110 mm

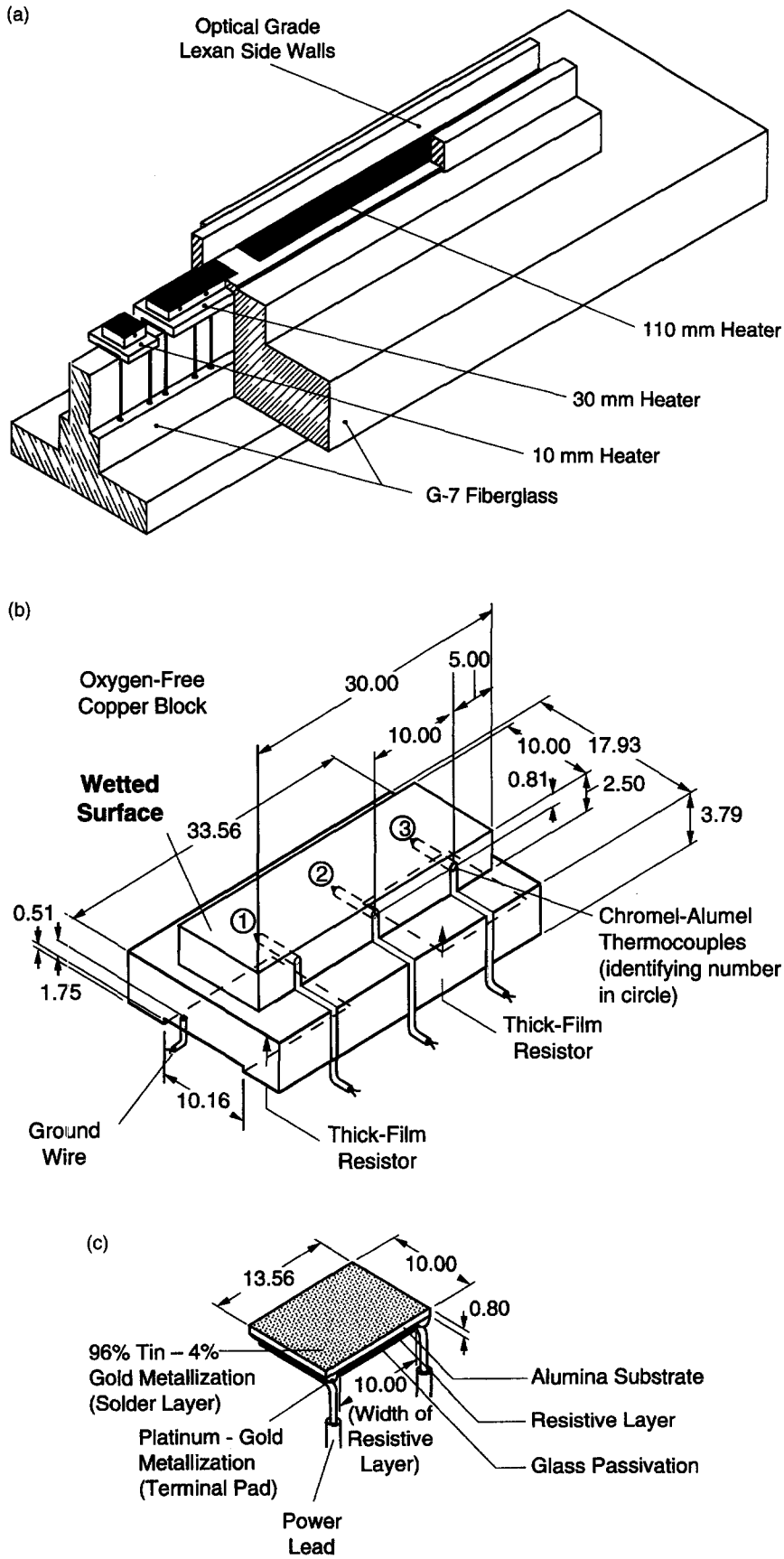

Fig. 3. Construction of (a) heater module, (b) 30 mm heater, and (c) thick film resistor.

heater. Thermocouples placed just beneath the heater surface, as shown in Fig. 3(b), were utilized to infer the surface temperature of the heaters from a one-dimensional heat conduction model. The total power generated by the resistors on each heater was measured with current and voltage transducers, and the heat flux on the surfaces of the two longer heaters was calculated by dividing the total energy generated by all the resistors by the total heater surface area. During a given test, only one of the three heaters was operated at a time so that the heaters did not affect each other.

2.3. *Test procedure and measurement uncertainty*

Prior to being set into the pool boiling facility, the heater surfaces were vapor blasted with a water-particulate spray consisting of particles with an average size of 10 μm. In the nucleate boiling region, the heat flux was increased and then the system was allowed to reach steady state before a measurement was taken. CHF was achieved when a large and rapid rise in surface temperature was experienced. Near CHF, small heat flux increments were used to ensure that CHF was not reached prematurely. In this study, CHF was denoted as the highest heat flux that gave a stable temperature reading plus one half of the last power increment. In order to protect the thick-film resistors from burnout, the data acquisition system was configured with relays to shut off all electrical power to the resistors once CHF was reached. Stable heat fluxes approximately equal to 95% of CHF are hereafter termed CHF−, and heat fluxes slightly greater than CHF, but less than a few seconds after the temperature excursion commences, are hereafter indicated as CHF+. For the current investigation, CHF data were repeatable to within $\pm 7\%$.

Propagation of error [26] was utilized in calculating the uncertainties associated with the experimental readings. All thermocouples were calibrated for a maximum uncertainty of $\pm 0.1^{\circ}$C. At heat fluxes close to CHF, the maximum uncertainty of the heat flux measurements obtained from the voltage and current transducers was estimated to be ± 1.0 W cm^{-2}.

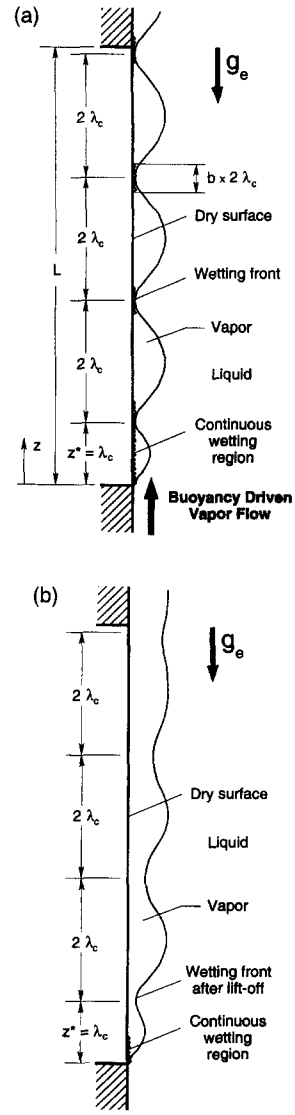

Fig. 4. Wetting front propagation along a vertical surface, shown at $t = 2\lambda_c/c_r$, for (a) CHF− and (b) CHF+.

3. PHOTOGRAPHIC STUDY OF VAPOR LAYER INTERFACIAL FEATURES

Still photography studies of the wall region revealed that at high heat flux conditions leading to CHF, the vertical pool boiling experiments exhibited vapor production behavior patterns similar to flow boiling experiments performed by Galloway and Mudawar [21] and Gersey and Mudawar [23]: (1) at a heat flux of about 85% of CHF, large coalescent bubbles were observed sliding over the heater surface; (2) the length of these coalescent bubbles increased with increasing heat flux until, eventually, a fairly continuous wavy vapor layer was formed over the heater surface at heat fluxes close to CHF−, as illustrated in Fig. 4(a); (3) boiling was sustained by liquid entrainment near the lower edge of the heater, as well as in *wetting fronts*, where the liquid–vapor interface made contact with the heater surface; (4) regions between neighboring wetting fronts experienced dry out; (5) CHF commenced when the liquid–vapor interface of the most upstream wetting front separated from the heater surface and (6) remaining wetting fronts were separated, in succession, after separation of the upstream wetting front, as illustrated in Fig. 4(b). Experimental evidence supporting this wetting front description is also available from flow boiling studies by Fiori and Bergles [27] and Hino and Ueda [28, 29], all of whom measured fluctuations in heater surface temperature synchronous with the passage of vapor slugs.

Still photographs of the near-wall interfacial features were made with a 35-mm Nikon camera with a 200 mm lens and a 1/64000 s, high intensity flash.

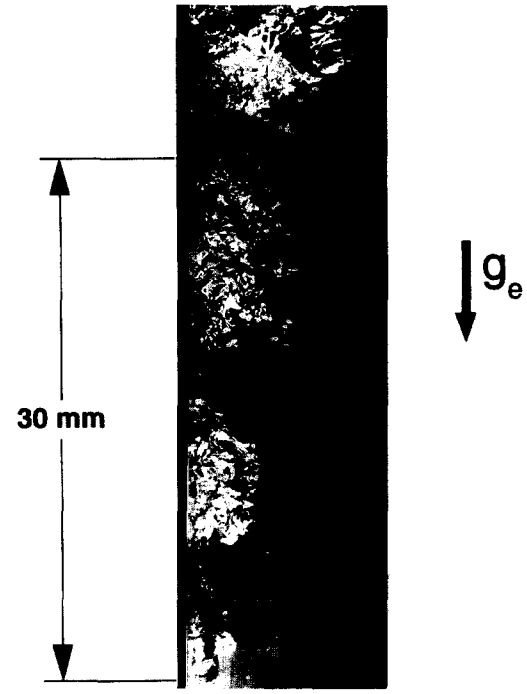

Fig. 5. Wavy vapor layer development just prior to CHF for vertical pool boiling on the 30 mm heater.

Figure 5 shows the wavy vapor layer formation on the 30 mm vertical heater corresponding to CHF−. Using a magnification better than 50×, no vapor jets could be seen emanating from the heater surface. Rather, a violent surge of small bubbles in the wetting fronts was observed to be feeding the vapor layer.

4. CHF MODEL

4.1. *Vapor wave and wetting front behavior*

The proposed CHF model is built upon physical observations from extensive video imaging and still photography studies as discussed in the previous section and illustrated in Fig. 4(a). At a reference time $t = 0$, a disturbance in the liquid–vapor interface having a wavelength equal to λ_c is assumed to touch the heater surface at $z = z^*$ (where z^* is equal to λ_c for pool boiling). This enables the liquid to contact the heater over a localized region. The wetting front then propagates along the heater surface at a speed c_r. A short time later, at $t = \lambda_c/c_r$, another disturbance approaches the heater surface at $z = z^*$ but is forced away by the momentum of vapor emanating from residual liquid left after the passage of the previous wetting front. Not until a later time, $t = 2\lambda_c/c_r$, after the residual liquid has been consumed at the location of the first wetting front, will a new wetting front be established on the heater surface. Wetting is, therefore, skipped every other cycle and wetting fronts are separated by $2\lambda_c$ wavelengths. The wave placement shown in both Figs. 4(a) and (b) is for time $t = 2\lambda_c/c_r$.

4.2. *Surface energy balance at CHF*

A Lagrangian frame of reference is used to model the heat transfer to the moving wetting fronts. Equation (2) sums the transient energy removed from the heater by the passage of all the wetting fronts in contact with the heater between the time a wetting front first forms on the heater surface and the time the next wetting front is established at the same location. Equation (2) also accounts for the steady heat removal from the continuous wetting zone, $0 < z < z^*$:

$$q_m = \frac{c_r/(2\lambda_c)}{L-z^*}\left[\int_0^\tau\int_{z^*}^L q_{s,1}\,dz\,dt+\cdots+\int_0^\tau\int_{z^*}^L q_{s,n}\,dz\,dt\right] \tag{2}$$

where $q_{s,1}, q_{s,2}, \ldots, q_{s,n}$ are the local heat fluxes corresponding to wetting 1, 2, ..., n, respectively. The local heat flux, q_s, is essentially zero where the heater surface is dry and is equal to some heat flux value, q_l, where a wetting front is present.

A photographic study of flow boiling by Galloway and Mudawar [21, 22] revealed that the span (length) of each wetting front, b, was one-fourth the separation distance between wetting fronts. Vertical pool boiling photographs from the current investigation exhibited the same trend in the wetting front span; i.e. CHF is about one-fourth the heat flux concentrated in the wetting fronts. A surface energy balance detailed by Galloway and Mudawar [22] reduces equation (2) to the following expression for CHF:

$$q_m = bq_l\left[1-\frac{\lambda_c}{16(L-z^*)}\right] \tag{3}$$

where the wetting front span, b, is equal to one-fourth, q_l is the localized heat flux at the wetting front, and the coefficient in the brackets accounts for continuous wetting in the region $0 < z < z^*$ and any partial wetting fronts in the downstream region and is close to unity for most operating conditions.

4.3. *CHF trigger mechanism: lift-off criterion*

CHF will commence when the upstream wetting front lifts off the heater surface. This occurs when the localized heat flux at the wetting front, q_l, is large enough that the normal momentum of vapor generated in the wetting front just exceeds the pressure force exerted upon the interface as a result of interfacial curvature:

$$\rho_g\left[\frac{q_l}{\rho_g h_{fg}\left(1+\dfrac{c_{p,f}\Delta T_{sub}}{h_{fg}}\right)}\right]^2 = \overline{P_f-P_g} \tag{4}$$

where the average pressure difference across the interface, $\overline{P_f-P_g}$, is calculated by integrating the pressure difference over the span of the most upstream wetting front. As lift-off occurs, the interface curvature is reduced and the vapor momentum flux increases, accelerating the interfacial lift-off even further.

Combining equations (3) and (4) and substituting one-fourth for the wetting front span yields an expression for CHF which is applicable to flow boiling for both straight and curved heaters, as shown by Galloway and Mudawar [22, 30] and Gersey and Mudawar [24], and to vertical pool boiling:

$$q_m = \frac{1}{4}\rho_g h_{fg}\left(1-\frac{\lambda_c}{16(L-z^*)}\right)\left(1+\frac{c_{p,f}\Delta T_{sub}}{h_{fg}}\right) \times\left[\frac{\overline{P_f-P_g}}{\rho_g}\right]^{1/2}. \quad (5)$$

Equation (5) shows predicting CHF requires estimation of $\overline{P_f-P_g}$. The next section will discuss an instability model which will be used to predict this key parameter.

4.4. *Interfacial instability of vapor layer*

The interfacial waviness illustrated in Fig. 4(a) can be idealized as a hydrodynamic instability of an interface between a vapor layer of velocity $\bar{u}_g$ and a liquid layer of velocity $\bar{u}_f$. Using classical instability theories [31, 32], the interfacial pressure difference resulting from a sinusoidal disturbance of the form $\eta(z,t)=\eta_0 e^{ik(z-ct)}$ perpendicular to the unperturbed interface can be expressed as:

$$P_f-P_g = -\eta k[\rho_f''(c-\bar{u}_f)^2+\rho_g''(\bar{u}_g-c)^2] -(\rho_f-\rho_g)g_n\eta = -\sigma k^2\eta \quad (6)$$

where g_n is the body force per unit mass perpendicular to the unperturbed interface, and the modified density terms for a straight heater can be expressed as $\rho_f''=\rho_f\coth(kH_f)$ and $\rho_g''=\rho_g\coth(kH_g)$, where H_f and H_g are the mean liquid and vapor layer thicknesses, respectively. Solving equation (6) for the wave speed, c, and utilizing the fact that for vertical pool boiling, $g_n=0$, $\bar{u}_f=0$, $\rho_f''=\rho_f$, and $\rho_g''\approx\rho_g$, the following equation results:

$$c=\frac{\rho_g\bar{u}_g}{(\rho_g+\rho_f)}\pm\sqrt{\frac{\sigma k}{(\rho_g+\rho_f)}-\frac{\rho_g\rho_f\bar{u}_g^2}{(\rho_g+\rho_f)^2}}. \quad (7)$$

When the liquid–vapor interface becomes unstable, c can be expressed as an imaginary number, with a real component:

$$c_r=\frac{\rho_g\bar{u}_g}{(\rho_g+\rho_f)} \quad (8)$$

and an imaginary component:

$$c_i=\sqrt{\frac{\rho_g\rho_f\bar{u}_g^2}{(\rho_g+\rho_f)^2}-\frac{\sigma k}{(\rho_g+\rho_f)}}. \quad (9)$$

The critical wavelength, or the wavelength that produces a neutrally stable wave, can be calculated by setting c_i in equation (9) equal to zero, such that:

$$\lambda_c=\frac{2\pi}{k_c}=\frac{2\pi\sigma(\rho_f+\rho_g)}{\rho_f\rho_g\bar{u}_g^2}. \quad (10)$$

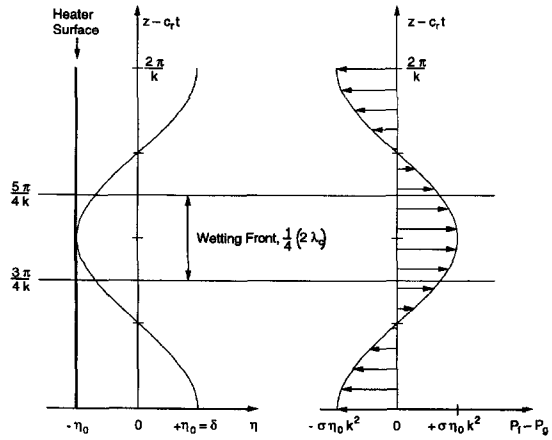

Fig. 6. Pressure distribution across a wetting front.

The interface instability analysis, and equation (9), demonstrate that surface tension is the stabilizing force, so longer wavelengths will become unstable first. However, close to the leading edge, where the velocity is small and thus the critical wavelength calculated from equation (10) is large, the wavelengths cannot exist because their lengths are larger than the corresponding stream-wise location. Therefore, the first critical wavelength that exists corresponds to the first wetting front and the stream-wise location z^*, as shown in Fig. 4(a).

Figure 6 shows how the interfacial curvature produces a pressure force on the interface which tends to maintain liquid contact with the heater surface in the trough regions of the waves. At the onset of instability the interfacial curvature of any wetting front can be described as a sinusoidal shape with a wavelength of $2\lambda_c$, or:

$$\eta(z,t)=\delta\cos[k(z-c_r t)] \quad (11)$$

where $k=2\pi/(2\lambda_c)$. By substituting equation (11) into equation (6), and integrating the pressure difference over the span of the most upstream wetting front, the mean interfacial force over the wetting front becomes:

$$\overline{P_f-P_g} = \frac{\int_{3\pi/4k}^{5\pi/4k}-\sigma\delta k^2\cos[k(z-c_r t)]\,d(z-c_r t)}{\frac{1}{4}(2\lambda_c)} = 2\sqrt{2\pi}\frac{\sigma\delta}{\lambda_c^2}. \quad (12)$$

Substituting the above expression in equation (5), and neglecting the coefficient due to the upstream continuous wetting zone and the downstream partial wetting fronts, gives:

$$q_m=\frac{1}{4}\rho_g h_{fg}\left[1+\frac{c_{p,f}\Delta T_{sub}}{h_{fg}}\right]\left[(2\sqrt{2\pi})\frac{\sigma\delta}{\rho_g\lambda_c^2}\right]^{1/2}. \quad (13)$$

The critical wavelength is determined from equation (10) where the mean vapor velocity, $\bar{u}_g$, and the vapor thickness, δ, are determined from the separated flow model described below.

4.5. *Separated flow model*

Applying mass and energy conservation for a control volume of the vapor layer of length dz, and then combining the two equations and integrating with respect to z, gives:

$$\rho_g \bar{u}_g \delta = \frac{q_m z}{h_{fg}\left[1+\frac{c_{p,f}\Delta T_{sub}}{h_{fg}}\right]}. \tag{14}$$

A momentum balance on the same control volume yields:

$$\frac{d}{dz}[\rho_g \bar{u}_g^2 \delta] = (\rho_f - \rho_g) g_e \delta - \tau_i - \tau_g\left(1+\frac{2\delta}{w}\right) \tag{15}$$

where the wall shear stress, τ_g, and the interfacial shear stress, τ_i, are defined as $\tau_g = 0.5 f_g \rho_g \bar{u}_g^2$ and $\tau_i = 0.5 f_i \rho_g \bar{u}_g^2$. The wall friction factor, f_g, can be predicted from the Blausius correlation for turbulent flow, $f_g = 0.0791/Re^{0.25}$, where Re is the Reynolds number based on the hydraulic diameter of the vapor layer, $2w\delta/(w+\delta)$. For the interfacial friction factor, Galloway and Mudawar [22] and Gersey and Mudawar [24] found that a constant value of $f_i = 0.5$ provided the best agreement between measured and predicted pressure drops obtained from flow boiling studies. It is important to point out that this value for f_i was determined for a range of heat flux values and has no bearing on the other sub-models used to predict CHF. For vertical pool boiling, a parametric study of f_i ranging from 0.25 to 1.0 indicated that the value of f_i does not significantly affect separated flow model results. Therefore, a value of $f_i = 0.5$ was utilized in the present study as well.

Combining equations (14) and (15) produces a differential equation relating $\bar{u}_g$ to z. The authors were unable to solve the resulting differential equation analytically, but found that the limiting case where the wall shear stress and the momentum gradient in equation (15) are neglected closely approximates the numerical solution for the two fluids examined in the current investigation, water and FC-72 at 1 atmosphere. For this limiting case, $\bar{u}_g$ can be approximated as:

$$\bar{u}_g = \left[\left(\frac{\rho_f-\rho_g}{\rho_g}\right) g_e \frac{q_m}{0.5 f_i \rho_g h_{fg}\left[1+\frac{c_{p,f}\Delta T_{sub}}{h_{fg}}\right]} z\right]^{1/3}. \tag{16}$$

Details of the numerical solution and the limiting cases examined can be found in the Appendix.

Substituting the above equation for the mean vapor velocity, $\bar{u}_g$, into the combined mass and energy conservation equation (14) gives the variation of vapor thickness, δ, with the stream-wise distance, z:

$$\delta = \frac{q_m}{\rho_g h_{fg}\left[1+\frac{c_{p,f}\Delta T_{sub}}{h_{fg}}\right]}\left[\left(\frac{\rho_f-\rho_g}{\rho_g}\right) \times g_e \frac{q_m}{0.5 f_i \rho_g h_{fg}\left[1+\frac{c_{p,f}\Delta T_{sub}}{h_{fg}}\right]}\right]^{-1/3} z^{2/3}. \tag{17}$$

Since the first wetting front is established at $z = \lambda_c$, the critical wavelength equation (10) can be combined with the mean vapor velocity equation (16) corresponding to $z = \lambda_c$ and reduced to:

$$\lambda_c = \left[2\pi\sigma\left(\frac{\rho_f+\rho_g}{\rho_f\rho_g}\right)\right]^{3/5} \times \left[\left(\frac{\rho_f-\rho_g}{\rho_g}\right) g_e \frac{q_m}{0.5 f_i \rho_g h_{fg}\left[1+\frac{c_{p,f}\Delta T_{sub}}{h_{fg}}\right]}\right]^{-2/5}. \tag{18}$$

The current model assumes that the character of the wave is preserved downstream of the first wetting front. Thus, the critical wavelength does not vary with axial direction for z greater than λ_c.

4.6. *CHF prediction*

In order to obtain a closed form expression for q_m from equation (13), the expression for δ, equation (17), must be evaluated at some axial location. Galloway and Mudawar [22] observed that the wetting front formed at $z = \lambda_c$, but then propagated downstream a short distance before the liquid–vapor interface lifted from the heater surface. For the present model, δ was taken at an axial location of $3/2\lambda_c$, the average between the location where the wave is generated, $z = \lambda_c$, and the location of the wave peak, $z = 2\lambda_c$. Substituting the expressions for δ (based on $z = 3/2\lambda_c$) and λ_c, equations (17) and (18), respectively, into equation (13) and solving for q_m yields the following CHF relation:

$$q_m = 2^{-113/24} 3^{5/6}\left(\frac{\pi}{f_i}\right)^{1/4}\left[\frac{\rho_f}{\rho_f+\rho_g}\right]\rho_g h_{fg} \times \left[1+\frac{c_{p,f}\Delta T_{sub}}{h_{fg}}\right]\left[\frac{\sigma(\rho_f-\rho_g)g_e}{\rho_g^2}\right]^{1/4} \tag{19}$$

where $f_i = 0.5$. The above equation assumes that the waves are perfectly sinusoidal and repeatable, and that the liquid wets the surface continuously throughout the span of the wetting front. It also omits friction effects from the liquid moving in the wetting front, and does not account for the statistical spread of the vapor wavelength, λ_c, and the vapor wave thickness, δ. These effects contribute to the scatter observed in the experimental CHF values listed in Table 1.

The heat flux equation (19) can be further simplified for saturated conditions and pressures much smaller than critical to:

$$q_m = 0.151\rho_g h_{fg}\left[\frac{\sigma(\rho_f-\rho_g)g_e}{\rho_g^2}\right]^{1/4}. \quad (20)$$

Interestingly, equation (20) is identical in form to the non-dimensional form recommended by Kutateladze [1] and to the model by Zuber *et al.* [2], although the mechanisms proposed in the individual models are distinctly different. Also, while the model by Zuber *et al.* includes a gravity term normal to the heater surface, resulting in a prediction of zero CHF for vertical surfaces, the present model predicts a finite value for vertical pool boiling CHF.

It should be noted that the present model is only valid for near saturated conditions, since it does not account for condensation at the interface. Additionally, this model ignores conduction–convection contributions and thus is not valid for liquid metals.

5. RESULTS

If the closed form heat flux equation (19) is substituted into the critical wavelength equation (18), the critical wavelength can be reduced to:

$$\lambda_c = \frac{2^{25/12}}{3^{1/3}}(\pi f_i)^{1/2}\left[\frac{\rho_f+\rho_g}{\rho_f}\right]\left[\frac{\sigma}{(\rho_f-\rho_g)g_e}\right]^{1/2}. \quad (21)$$

Dividing the characteristic length, L, by the critical wavelength, λ_c, gives:

$$\frac{L}{\lambda_c} = \frac{3^{1/3}}{2^{25/12}}(\pi f_i)^{-1/2}L\left[\frac{\rho_f}{\rho_f+\rho_g}\right]\left[\frac{(\rho_f-\rho_g)g_e}{\sigma}\right]^{1/2}. \quad (22)$$

For pressures much smaller than critical, equation (22) produces the same grouping of parameters as the critical Taylor wavelength, which has often been used to non-dimensionalize the characteristic length of heaters in pool boiling CHF studies. That is,

$$\frac{L}{\lambda_c} \propto L' = L\left[\frac{(\rho_f-\rho_g)g_e}{\sigma}\right]^{1/2}. \quad (23)$$

Thus, the dimensionless characteristic heater length, L', described in equation (23) is valid for the present analysis even though it was derived in prior studies from the Taylor instability; the presence of the gravity term in the present model and in equation (23) results from the buoyancy driven vapor flow, not the Taylor instability.

The non-dimensional CHF pool boiling data obtained during the present investigation, along with data from Monde *et al.* [7], are plotted in Fig. 7 with respect to the dimensionless characteristic heater length, L'. CHF data obtained from thin heaters [4, 6] were not included because the low thermal capacity of thin heaters results in reduced CHF values [33]. Additionally, liquid helium and liquid nitrogen CHF values were excluded from Fig. 7 because of the lack of measurement accuracy inherent with cryogenic experiments. The average of the 27 non-dimensional vertical pool boiling CHF data shown in Fig. 7 is $K = 0.155$, with a standard deviation of 0.015, which is very close to the model prediction of $K = 0.151$ obtained from equation (20). Although the average non-dimensional CHF value does not change much if the cryogenic CHF data are included (K becomes 0.154), the standard deviation of the data becomes 0.021, indicating that the scatter in the data is greater if cryogenic fluids are included. Because of the stretching and merging of waves as they travel downstream, the dimensionless CHF, K, decreases slightly with the dimensionless characteristic heater length, L'. However, since this effect is small, it has been neglected for the current analysis.

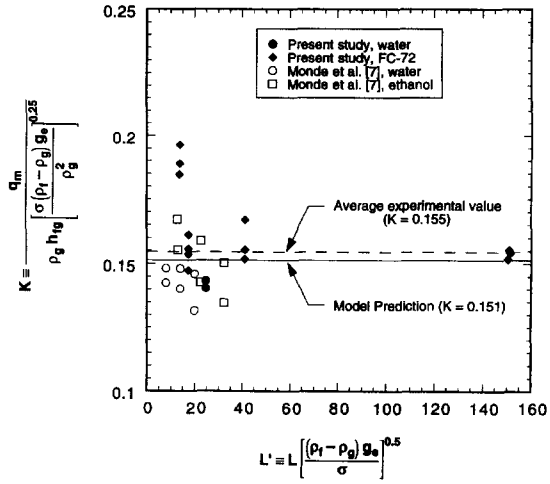

Fig. 7. Dimensionless CHF data plotted with respect to dimensionless characteristic heater length.

The lengths of the liquid–vapor waves were measured from still photographs of the 10, 30 and 110 mm heaters. The wavelengths were measured from trough to trough, and the stream-wise location of the peak of the wave was taken as the z location of the wave. Because of the statistical scatter of the wavelengths, the data were sorted into 1 mm bins and the percentage of wavelengths in each bin were calculated and are shown in Fig. 8. The wavelengths were segregated by stream-wise position into two groups. For the first group, $0 < z < 10$ mm, the majority of the wavelengths were close to $2\lambda_c$, which is consistent with the current model. As the waves traveled downstream, they stretched and merged with other waves, so the majority of the wavelengths of the second group, $10 < z < 50$ mm, were close to $4\lambda_c$. Because of the large wavelengths at the far downstream positions there was not enough data in the region where z was larger than 50 mm to statistically determine anything conclusively, so this data was omitted from the plot. These results explain why CHF values for long heaters tend to be somewhat smaller than for short heaters in vertical pool boiling.

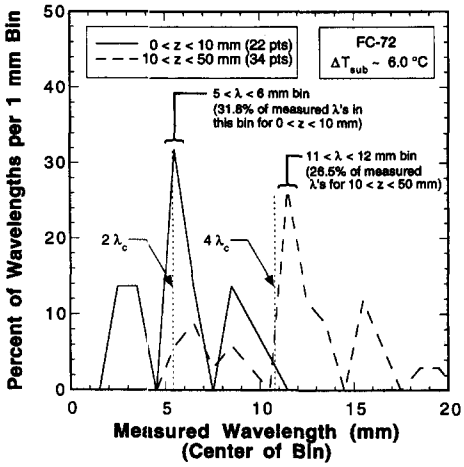

Fig. 8. Histogram of measured wavelengths segregated by stream-wise position.

6. CONCLUSIONS

Experiments involving pool boiling from vertical surfaces were performed to ascertain the CHF trigger mechanism. Key conclusions from the study are as follows:

(1) At high heat flux conditions, vertical pool boiling exhibits vapor production and vapor flow patterns similar to those found in flow boiling.

(2) A fairly continuous wavy vapor layer engulfs the heater surface at heat fluxes slightly smaller than CHF. Boiling remains active in the wetting fronts, where the interface of the vapor layer contacts the heater surface. CHF is triggered when the normal momentum of the vapor produced in the wetting front exceeds the pressure force exerted upon the interface due to interfacial curvature.

(3) For pressures much smaller than critical, the dimensionless characteristic heater length produced from the current analysis based on the Helmholtz instability is the same as the dimensionless length produced from an analysis based on the Taylor instability. The presence of the gravity terms in the present analysis is due to the buoyancy effects responsible for vapor flow, not to the Taylor instability.

(4) The present pool boiling CHF model reduces to an expression identical in form to the models by Kutateladze [1] and Zuber *et al.* [2], although the mechanisms proposed in the individual models are distinctly different. Additionally, while the model by Zuber *et al.* [2] includes a gravity term normal to the heater surface, resulting in a prediction of zero CHF for vertical surfaces, the present model predicts a finite value for vertical pool boiling CHF.

Acknowledgements—The authors gratefully acknowledge the support of the Office of Basic Energy Sciences of the U.S. Department of Energy (Grant No. DE-FE02-93ER14394). The authors also thank the Industrial Chemical Products Division of 3M Company for donating Florinert FC-72 for the present study.

REFERENCES

1. S. S. Kutateladze, On the transition to film boiling under natural convection, *Kotloturbostroenie* **3,** 10–12 (1948).
2. N. Zuber, M. Tribus and J. W. Westwater, The hydrodynamic crisis in pool boiling of saturated and subcooled liquids, *Int. Dev. Heat Transfer: Proceedings of the* 1961–62 *International Heat Transfer Conference*, Boulder, CO, pp. 230–236 (1961).
3. T. D. Bui and V. K. Dhir, Transition boiling heat transfer on a vertical surface, *ASME J. Heat Transfer* **107,** 756–763 (1985).
4. J. H. Lienhard and V. K. Dhir, Hydrodynamic prediction of peak pool-boiling heat fluxes from finite bodies, *ASME J. Heat Transfer* **95,** 477–482 (1973).
5. J. M. Adams, A study of the critical heat flux in an accelerating pool boiling system, Ph.D. Thesis, University of Washington, Seattle, WA (1962).
6. I. P. Vishnev, I. A. Filatov, Y. G. Vinokur, V. V. Gorokhov and G. G. Svalov, Study of heat transfer in boiling of helium on surfaces with various orientations, *Heat Transfer—Sov. Res.* **8**(4), 104–108 (1976).
7. M. Monde, H. Kusuda and H. Uehara, Critical heat flux during natural convective boiling in vertical rectangular channels submerged in saturated liquid. *ASME J. Heat Transfer* **104,** 300–303 (1982).
8. C. Beduz, R. G. Scurlock and A. J. Sousa, Angular dependence of boiling heat transfer mechanisms in liquid nitrogen, *Adv. Cryog. Engng* **33,** 363–370 (1988).
9. C. J. Chui, M. S. Sehmbey, L. C. Chow and O. J. Hahn, Pool boiling heat transfer from a vertical heater array in liquid nitrogen, *Proceedings of the 6th AIAA/ASME Joint Thermophysics and Heat Transfer Conf.*, AIAA-94-1992, Colorado Springs, CO (1992).
10. S. S. Kutateladze and A. I. Leont'ev, Some applications of the asymptotic theory of the turbulent boundary layer, *1966 Heat Transfer Conference, Proceedings of the Third International Heat Transfer Conference*, Chicago, IL, Vol. 3, pp. 1–6 (1966).
11. L. S. Tong, Boundary-layer analysis of the flow boiling crisis, *Int. J. Heat Mass Transfer* **11,** 1208–1211 (1968).
12. L. S. Tong, A phenomenological study of critical heat flux, ASME Paper 75-HT-68 (1975).
13. J. H. Lienhard and R. Eichhorn, Peak boiling heat flux on cylinders in a cross flow, *Int. J. Heat Mass Transfer* **19,** 1135–1142 (1976).
14. J. H. Lienhard and M. Hasan, On predicting boiling burnout with the mechanical energy stability criterion, *ASME J. Heat Transfer* **101,** 276–279 (1979).
15. G. J. Kirby, R. Staniforth and J. H. Kinneir, A visual study of forced convection boiling—II. Flow patterns and burnout for a round test section, Report AEEW-R 506, United Kingdom Atomic Energy Authority Reactor, Winfrith, United Kingdom (1967).
16. W. Hebel, W. Detavernier and M. Decreton, A contribution to the hydrodynamics of boiling crisis in a forced flow of water, *Nucl. Engng Des.* **64,** 433–445 (1981).
17. J. Weisman and B. S. Pei, Prediction of critical heat flux in flow boiling at low qualities, *Int. J. Heat Mass Transfer* **26,** 1463–1477 (1983).
18. C. H. Lee and I. Mudawar, A mechanistic critical heat flux model for subcooled flow boiling based on local bulk flow conditions, *Int. J. Multiphase Flow* **14,** 711–728 (1988).
19. Y. Katto, A physical approach to critical heat flux of subcooled flow boiling in round tubes, *Int. J. Heat Mass Transfer* **33,** 611–620 (1990).
20. Y. Katto, Prediction of critical heat flux of subcooled flow boiling in round tubes, *Int. J. Heat Mass Transfer* **33,** 1921–1928 (1990).
21. J. E. Galloway and I. Mudawar, CHF mechanism in flow boiling from a short heated wall—I. Examination of near-wall conditions with the aid of photo-

micrography and high speed video imaging, *Int. J. Heat Mass Transfer* **36,** 2511–2526 (1993).
22. J. E. Galloway and I. Mudawar, CHF mechanism in flow boiling from a short heated wall—II. Theoretical CHF model, *Int. J. Heat Mass Transfer* **36,** 2527–2540 (1993).
23. C. O. Gersey and I. Mudawar, Effects of heater length and orientation on the trigger mechanism for flow boiling CHF—I. Photographic study and statistical characterization of the near-wall interfacial features, *Int. J. Heat Mass Transfer* **38,** 629–641 (1995).
24. C. O. Gersey and I. Mudawar, Effects of heater length and orientation on the trigger mechanism for flow boiling CHF—II. CHF model, *Int. J. Heat Mass Transfer* **38,** 643–654 (1995).
25. S. Reed and I. Mudawar, Enhancement of boiling heat transfer using highly wetting liquids with pressed-on fins at low contact forces, *Int. J. Heat Mass Transfer* **40,** 2379–2392 (1997).
26. R. J. Moffat, Describing the uncertainties in experimental results, *Exp. Thermal Fluid Sci.* **1,** 3–17 (1988).
27. M. P. Fiori and A. E. Bergles, Model of critical heat flux in subcooled flow boiling, *Proceedings of the 4th International Heat Transfer Conference*, Paris/Versailles, France, Vol. VI, pp. 354–365 (1970).
28. R. Hino and T. Ueda, Studies on heat transfer and flow characteristics in subcooled flow boiling—I. Boiling characteristics, *Int. J. Multiphase Flow* **11,** 269–281 (1985).
29. R. Hino and T. Ueda, Studies on heat transfer and flow characteristics in subcooled flow boiling—II. Flow characteristics, *Int. J. Multiphase Flow* **11,** 283–297 (1985).
30. J. E. Galloway and I. Mudawar, A theoretical model for flow boiling CHF from short concave heaters, *ASME J. Heat Transfer* **117,** 698–707 (1995).
31. H. Lamb, *Hydrodynamics* (6th Edn), p. 371. Dover Publications, New York (1945).
32. L. M. Milne-Thompson, *Theoretical Hydrodynamics* (4th Edn), p. 409. Macmillan, New York (1960).
33. W. R. Houchin and J. H. Lienhard, Boiling burnout in low thermal capacity heaters, ASME Paper 66-WA/HT-40 (1966).

APPENDIX

Equations (14) and (15) were combined along with the expressions for interfacial and wall shear stress to produce the following differential equation relating $\bar{u}_g$ to z:

$$\frac{\mathrm{d}}{\mathrm{d}z}[\bar{u}_g z] = \frac{(\rho_f-\rho_g)g_e}{\rho_g}\frac{z}{\bar{u}_g} - 0.5 f_i \rho_g \bar{u}_g^2 \frac{h_{fg}\left[1+\frac{c_{p,f}\Delta T_{sub}}{h_{fg}}\right]}{q_m} - 0.5 f_g \rho_g \bar{u}_g^2 \left(1+\frac{2q_m z}{w\rho_g \bar{u}_g h_{fg}\left[1+\frac{c_{p,f}\Delta T_{sub}}{h_{fg}}\right]}\right) \times \frac{h_{fg}\left[1+\frac{c_{p,f}\Delta T_{sub}}{h_{fg}}\right]}{q_m} \quad \text{(A1)}$$

where $f_i = 0.5$ and f_g can be expressed as:

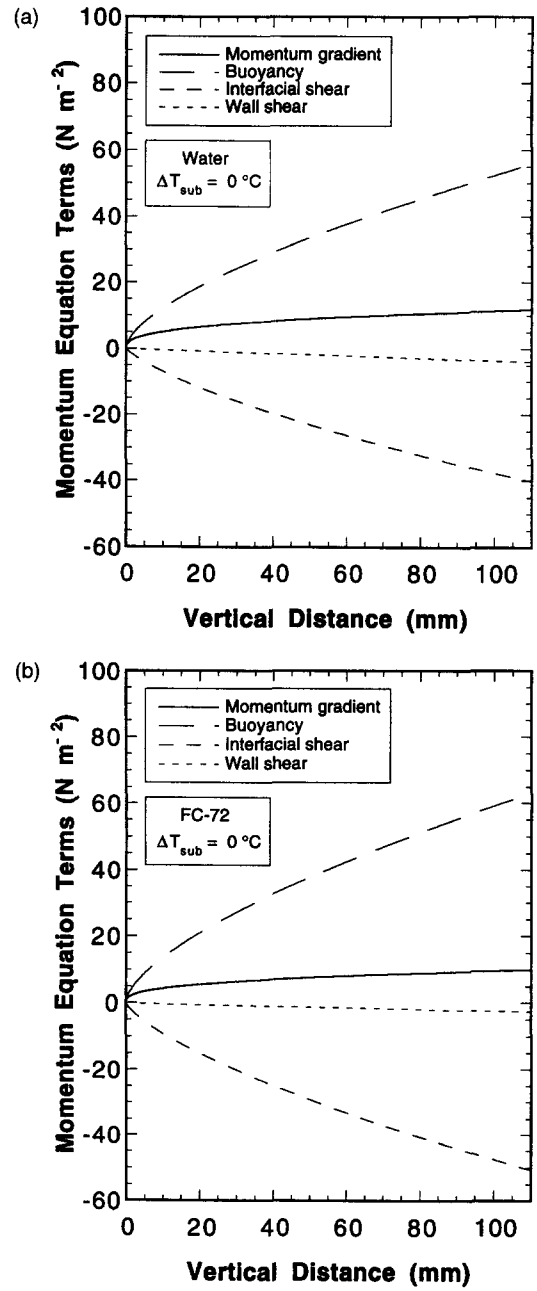

Fig. A1. Comparison of terms in the momentum balance, equation (15), for (a) water and (b) FC-72.

$$f_g = 0.0791\left[\frac{q_m z}{\mu_g h_{fg}\left[1+\frac{c_{p,f}\Delta T_{sub}}{h_{fg}}\right]}\right] \times \left[\frac{2w}{\left(w+\frac{q_m z}{\rho_g \bar{u}_g h_{fg}\left[1+\frac{c_{p,f}\Delta T_{sub}}{h_{fg}}\right]}\right)}\right]^{-0.25} \quad \text{(A2)}$$

Equation (A1) was solved numerically with a 4th-order

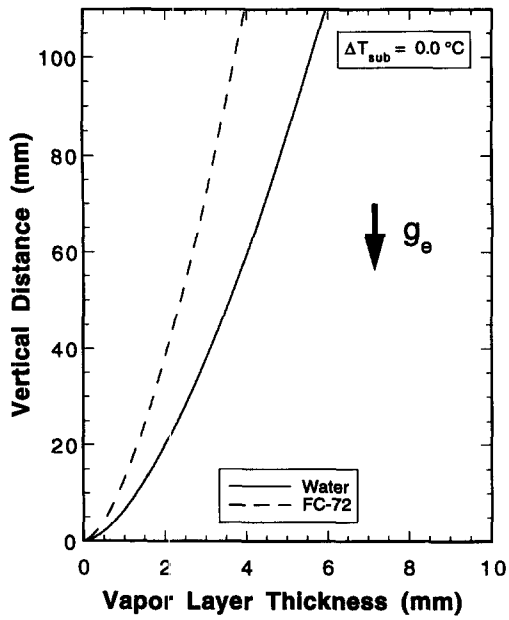

Fig. A2. Numerical vapor layer thickness for water and FC-72.

Runge–Kutta routine for both water and FC-72 at 1 atm, using experimental values for the maximum heat flux, q_m. The stream-wise step size of 0.0001 m provided an accuracy of ± 0.01 m s^{-1} for the velocity solution. The code was verified by solving equation (A1) both analytically and numerically for the limiting case when both shear terms are neglected. The numerical results agreed well with the analytical solution.

Based upon the numerical results, the four terms in equation (15) are plotted in Figs. A1(a) and (b) for water and FC-72, respectively. The momentum term, $d/dz[\rho_g \bar{u}_g^2 \delta]$, was determined from a first order central differencing scheme. For illustrative purposes the water solution was extended to 110 mm in length even though the heater from the actual experiment was only 62.0 mm. Figures A1(a) and (b) indicate that the wall shear stress is negligible. Figure A2 shows the vapor layer thickness predicted from the numerical solution. As expected, the water vapor layer was thicker than the FC-72 vapor layer profile because the term $(\rho_f - \rho_g)/\rho_g$ is larger for water.

In addition to the numerical solution, two limiting cases were examined which produced analytical solutions. If shear stresses are neglected and equations (14) and (15) are combined and solved, $\bar{u}_g$ can be expressed as:

$$\bar{u}_g = \left[\frac{2}{3}\left(\frac{\rho_f - \rho_g}{\rho_g}\right) g_e z\right]^{1/2}. \tag{A3}$$

If the wall shear stress and the momentum gradient are neglected in equation (15), $\bar{u}_g$ becomes:

$$\bar{u}_g = \left[\left(\frac{\rho_f - \rho_g}{\rho_g}\right) g_e \frac{q_m}{0.5 f_i \rho_g h_{fg}\left[1 + \frac{c_{p,f}\Delta T_{sub}}{h_{fg}}\right]} z\right]^{1/3}. \tag{A4}$$

Figures A3(a) and (b) show the comparison of the mean vapor velocities produced from the numerical solution of equation (A1) and from the limiting cases of negligible friction, equation (A3), and negligible momentum gradient, equation (A4), for both water and FC-72. Since the limiting

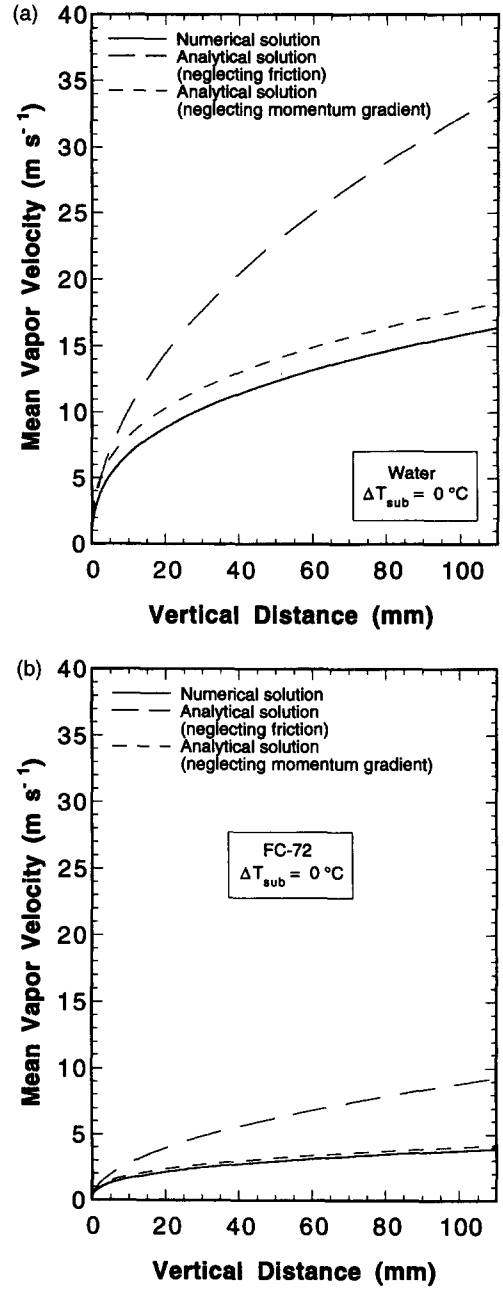

Fig. A3. Mean vapor velocity obtained numerically and analytically for (a) water and (b) FC-72.

case of negligible momentum gradient, equation (A4), comes closest to approximating the numerical solution for water and FC-72 at 1 atm, it was chosen for the analysis described within the paper. For completeness, if the same analysis was carried out with equation (A3) rather than equation (A4), the following CHF relation is obtained:

$$q_m = 2^{-7/2} \cdot (3\pi)^{1/4}\left[1 + \frac{c_{p,f}\Delta T_{sub}}{h_{fg}}\right]\left[\frac{\rho_f}{\rho_f + \rho_g}\right]^{3/4} \times \rho_g h_{fg}\left[\frac{\sigma(\rho_f - \rho_g) g_e}{\rho_g^2}\right]^{1/4}. \tag{A5}$$